Gas flows through shallow T-junctions and parallel microchannel networks

A. D. Gat,[a] I. Frankel, and D. Weihs
Faculty of Aerospace Engineering, Technion-Israel Institute of Technology, Haifa 32000, Israel

(Received 19 February 2010; accepted 28 July 2010; published online 30 September 2010)

We apply a recent extension of the Hele-Shaw scheme to analyze steady compressible viscous flows through micro T-junctions. The linearity of the problem in terms of an appropriately defined quadratic form of the pressure facilitates the definition of the viscous resistance of the configuration, relating the gas mass-flow rate to entrance and exit conditions. Furthermore, under rather mild restrictions, the performance of complex microchannel networks may be estimated through superposition of the contributions of multiple basic junction elements. This procedure is applied to an optimization model problem of a parallel microchannel network. The analysis and results are readily adaptable to incompressible flows. © *2010 American Institute of Physics*.
[doi:10.1063/1.3481386]

I. INTRODUCTION

Junctions connecting microchannels are common elements of considerable importance in microfluidic devices and occur in a variety of applications (e.g., mixing,[1–3] emulsification,[4–6] gas distribution systems,[7–9] etc.). Liquid flows through T-junctions have been studied via a combination of numerical simulations and experimental (micro particle image velocimetry) methods.[10,11] We focus here on gas flows, obtaining analytic approximations for the mass-flow rate through the junctions, which are then applied to estimate and optimize the performance of more complex network configurations.

The use of current microfabrication technologies often results in shallow planar configurations where fluid motion takes place within the narrow gap between parallel planes. Owing to the large surface-to-volume ratio associated with the small length scales, these flows are nearly isothermal[12,13] and the dominant balance involves pressure gradients and viscous resistance. This balance gives rise to so-called low-Mach compressibility, i.e., significant density variations which are only accompanied by minor fluid accelerations. Furthermore, under standard atmospheric conditions the Knudsen number (the ratio of the molecular mean free path to half the microchannel depth) is typically $Kn \approx 0.01-0.1$, corresponding to the slip-flow regime.[14]

In the next section we outline our recent extension of the Hele-Shaw scheme[15,16] which is then applied to the study of the compressible viscous flow through a shallow T-junction. The analytic expressions thus obtained serve to define and quantify the viscous resistance of the junction. In Sec. III we illustrate the use of these results to the evaluation of the performance of more complex channel-network configurations. A brief conclusion follows in Sec. IV. The relaxation to a uniform flow across straight channel segments is discussed in the Appendix.

[a]Present address: Department of Applied Physics, California Institute of Technology, Pasadena CA 91125, USA.

II. GAS FLOWS THROUGH SHALLOW T-JUNCTIONS

We consider a steady compressible viscous flow through the T-junction schematically depicted in Fig. 1(a). The junction of uniform depth $2H$ connects three straight channels of uniform widths $W_{BC}=W$, W_{EF}, and W_{GH}, respectively. Gas may enter or leave the junction through any of the connected channels. The illustration describes outfluxes $\dot{m}$ through BC and $(Q-1)\dot{m}$ through GH and (by mass conservation) an influx $Q\dot{m}$ through EF. However, all possible situations and geometries may be represented by appropriately selecting the various widths and adjusting the value of the parameter Q which may take any real, positive or negative, value. We select a Cartesian system of coordinates whose x,y axes lie at the configuration midplane and z is perpendicular thereto. In subsequent analysis the x,y coordinates are normalized by W and z by H.

Since the dominant balance involves the pressure gradients and viscous resistance, we scale the x,y components of the fluid velocity by $U=p_0H^2/\mu W$, where p_0 is a characteristic pressure drop and μ denotes the fluid viscosity. The z-component is accordingly normalized by UH/W. We here focus on low-Reynolds-number flows,[12,13] $\mathrm{Re}=\rho_0 UH/\mu \ll 1$, (where ρ_0 is the gas density at the reference pressure) through shallow configurations, i.e., when

$$\frac{H}{W}=\varepsilon \ll 1. \tag{1}$$

Within the above scaling the steady isothermal gas motion is to leading order governed by the dimensionless equation of continuity

$$\frac{\partial}{\partial x}(\rho u)+\frac{\partial}{\partial y}(\rho v)+\frac{\partial}{\partial z}(\rho w)=0 \tag{2}$$

the Cartesian components of the equation of motion

$$\frac{\partial p}{\partial x}=\frac{\partial^2 u}{\partial z^2}+O(\varepsilon\,\mathrm{Re},\varepsilon^2), \tag{3}$$

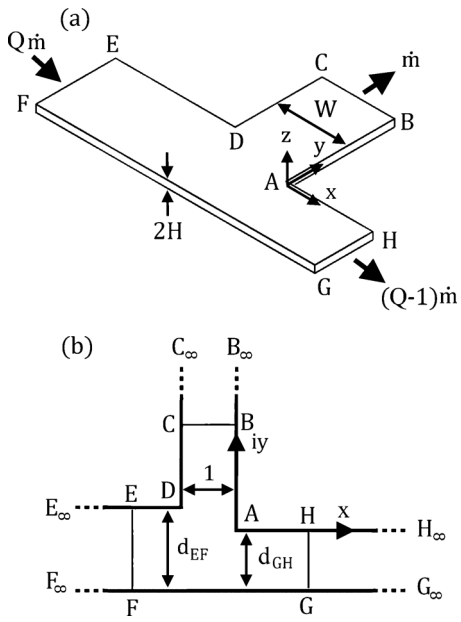

FIG. 1. A schematic description of (a) the shallow junction geometry and (b) the corresponding planform domain.

$$\frac{\partial p}{\partial y} = \frac{\partial^2 v}{\partial z^2} + O(\varepsilon\ \mathrm{Re}, \varepsilon^2), \tag{4}$$

and

$$\frac{\partial p}{\partial z} = O(\varepsilon^3\ \mathrm{Re}, \varepsilon^2) \tag{5}$$

together with the equation of state of a perfect isothermal gas

$$p = \rho. \tag{6}$$

At the small values of the Knudsen number typical of gas flows through shallow microconfigurations the above are supplemented by boundary conditions imposing the vanishing of normal velocities and Navier-type conditions[14] specifying the tangential velocity slip at solid walls, as well as appropriate conditions regarding the pressure or mass-flux density distribution across entrance and exit sections. Equation (5) implies a uniform pressure across the channel depth. The standard lubrication-approximation argument then allows for the integration of the remaining components, Eqs. (3) and (4), to express $\mathbf{u}_\parallel$, the in-plane velocity vector, in terms of $\nabla_\parallel p$, where $\nabla_\parallel = (\partial/\partial x, \partial/\partial y)$ is the planar portion of the gradient operator. Subsequent analysis of the present compressible viscous-flow problem is facilitated in terms of the quadratic form

$$G(x,y) = \tfrac{1}{6}p^2 + \lambda Kn_0 p \tag{7}$$

defined within the two-dimensional planform domain formed by the intersection of the configuration midplane and its lateral walls. In Eq. (7) Kn_0 denotes the value of Kn at the reference conditions and λ is the viscous-slip coefficient[14] (≈ 1.14). From Eq. (6), Eq. (7) and the above-mentioned expression of $\mathbf{u}_\parallel$ in terms of $\nabla_\parallel p$ one obtains the integral relation

$$\int_0^1 \rho \mathbf{u}_\parallel dz = -\nabla_\parallel G. \tag{8}$$

Thus $G(x,y)$ represents the scalar potential of the planar mass-flux density vector. For $\varepsilon, \mathrm{Re} \ll 1$ we put forward the asymptotic expansion

$$G \sim G_0 + \varepsilon \bar{c} G_1 + O(\varepsilon^2, \varepsilon\ \mathrm{Re}). \tag{9}$$

Our recent analysis[15] has established that G_0 and G_1 are both harmonic within the planform domain

$$\nabla_\parallel^2 G_0 = 0, \tag{10a}$$

$$\nabla_\parallel^2 G_1 = 0. \tag{10b}$$

At the lateral walls they satisfy the respective Neumann conditions

$$\frac{\partial G_0}{\partial n} = 0 \tag{11a}$$

and

$$\frac{\partial G_1}{\partial n} = \frac{\partial^2 G_0}{\partial s^2}, \tag{11b}$$

where n and s are the local normal and tangential coordinates at the lateral walls. By Eqs. (8) and (9) these are supplemented by appropriate Neumann or Dirichlet conditions at the entrance and exit sections according as the pressure or mass-flux density distributions are specified there [see Eqs. (12) and (13)]. The $O(1)$ parameter $\bar{c}$ represents the effects of the lateral-wall geometry (e.g., $\bar{c} \approx 0.63$ for rectangular cross sections[15]).

Calculation of G_0 and G_1 in the present problem is simplified by replacing the actual entrance (EF) and exit (BC and GH) sections by straight and uniform semi-infinite channels [cf. Fig. 1(b)]. With increasing distance upstream and downstream of the junction we anticipate that G becomes uniform across the width of these semi-infinite channels (see the Appendix). For the present configuration with (dimensionless) mass-flow rate $\dot{m} = 1$ at $B_\infty C_\infty$, we obtain the far-field conditions

$$\frac{\partial G_0}{\partial n} = \frac{Q}{d_{EF}}, \quad -\frac{Q-1}{d_{GH}}, \quad \text{and} \quad -1, \tag{12}$$

and

$$\frac{\partial G_1}{\partial n} = \frac{2Q}{d_{EF}^2}, \quad -\frac{2(Q-1)}{d_{GH}^2}, \quad \text{and} \quad -2 \tag{13}$$

across $E_\infty F_\infty$, $G_\infty H_\infty$, and $B_\infty C_\infty$, respectively. The general three-dimensional nonlinear compressible viscous-flow problem has thus been reduced to a pair of two-dimensional Neumann problems which, for a given planform geometry, need to be solved just *once*. In terms of G the above problem formulation remains essentially the same for viscous incompressible flows,[15] provided that we modify the definition (7) to $G = p/3$. It is useful to note that compressibility (as well as rarefaction) effects are implicit in the definition of G. They only become explicit when subsequent results are expressed in terms of the pressure.

To calculate G_0 and G_1 we apply the Schwarz–Christoffel theorem to obtain the conformal transformation

$$T(\zeta)=\frac{2i}{\pi}\left[d_{EF}\tan^{-1}(\sqrt{\zeta})+\tanh^{-1}\left(\sqrt{\frac{\zeta}{b}}\right)+d_{HG}\tan^{-1}\left(\sqrt{\frac{\zeta}{a}}\right)\right] \tag{14}$$

mapping the planform domain in the physical $t=x+iy$ plane onto the upper half of the auxiliary complex $\zeta=\xi+i\eta$ plane. The transformation parameters a, b appearing in Eq. (14) are related to the geometric features of the junction through

$$d_{EF}=\frac{a+b}{(1-a)\sqrt{b}} \quad \text{and} \quad d_{HG}=\frac{(b+1)\sqrt{a}}{(1-a)\sqrt{b}}. \tag{15}$$

In the ζ-plane G_0 is readily obtained as the real part of the analytic function

$$F_0(\zeta)=-\frac{1}{\pi}\left[Q\ln(1+\zeta)-\ln\left(1-\frac{\zeta}{b}\right)-(Q-1)\ln\left(1+\frac{\zeta}{a}\right)\right]. \tag{16}$$

By use of this together with Green's function for the Neumann problem in the upper half plane we obtain

$$G_1(\zeta)=-\frac{2}{\pi}\left[\frac{Q}{d_{EF}}\ln|1+\zeta|-\ln\left|1-\frac{\zeta}{b}\right|-\frac{(Q-1)}{d_{GH}}\ln\left|1+\frac{\zeta}{a}\right|\right]+\frac{1}{2\pi}\int_{-\infty}^{\infty}\left\{\frac{\partial}{\partial\beta}\left[\frac{F_0'(\beta)}{|T'(\beta)|}\right]\ln\left[\frac{(\xi-\beta)^2+\eta^2}{\beta^2}\right]\right\}d\beta. \tag{17}$$

Figure 2 illustrates the flow through the junction for $d_{GH}=1$, $d_{EF}=1.5$, and $Q=2.5$ (a), 1.42 (b), and 1.25 (c) for $\varepsilon\to 0$ (so that $G\sim G_0$). Presented are the streamlines (solid lines), isobars (i.e., level lines of G_0, dashed) and arrows indicating the location of the stagnation points. Unlike inertia-dominated isentropic flows these correspond to saddle points rather than maxima of the pressure distribution. Since the lateral walls are mapped on the real ξ axis in the ζ-plane, the location $(\xi_s,0)$ of the stagnation points is obtained from $\partial G_0/\partial\xi=0$ yielding

$$\xi_s=\frac{b(a-1)Q+(a+b)}{(a-1)Q-(a+b)}. \tag{18}$$

Thus, for a specific geometry (given a and b) ξ_s is determined by the value of Q, $Q=(a+b)/b(1-a)$ yielding $\xi_s=0$ corresponding to a stagnation point right at the corner of the junction [Fig. 2(b)]. For $Q\geq 1$ the specific value of Q determines the division of the mass outflux between the exit sections $G_\infty H_\infty$ and $B_\infty C_\infty$, respectively [(see Fig. 1(b)]. As illustrated in Fig. 2, the dividing streamline meeting the lateral wall at the stagnation point is thus shifting toward $B_\infty C_\infty$ with increasing Q and toward $G_\infty H_\infty$ with Q diminishing. Finally, for future reference it is useful to note that within a single channel width upstream or downstream of the junction, G already becomes nearly uniform across the channel which [by Eq. (8)] implies that the same is true of the fluid mass-flux density. This is further discussed in the Appendix.

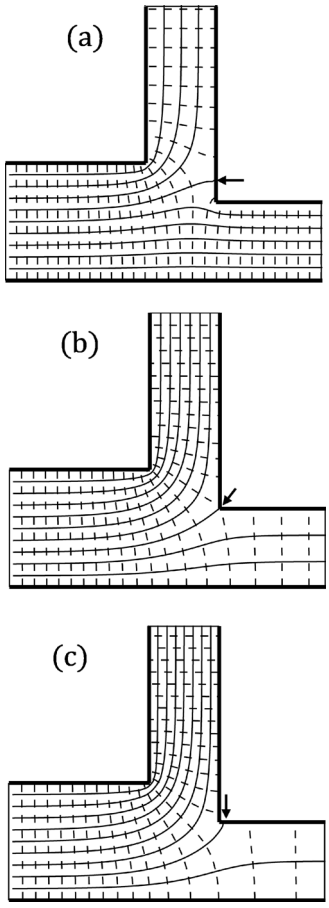

FIG. 2. Streamline (solid lines) and isobar (dashed lines) patterns for junctions characterized by $d_{EF}=1.5$ and $d_{GH}=1$ for (a) $Q=2.5$, (b) 1.42, and (c) 1.25.

Typical of compressible flows is the nonlinear streamwise variation of the pressure which stands in the way of the definition of the configuration viscous resistance as an intrinsic property of its geometry. However, the linearity of the problem in terms of the quadratic form G allows for the proportionality relation

$$G_{EF}-G_{BC}=\dot{m}R(Q,d_{EF},d_{HG},L_{EF},L_{HG},L_{BC};\varepsilon,\bar{c}) \tag{19a}$$

involving the difference between the (presumed uniform) entrance and exit values of G and the mass flow rate $\dot{m}$ (normalized by $2H^3p_0\rho_0/\mu$). The proportionality coefficient which depends on the geometric features of the configuration (see Fig. 3) and the parameter Q effectively represents the viscous resistance between the entrance (EF) and exit (BC) sections. Based on appropriate reinterpretation of the parameters one obtains the corresponding resistance between HG and BC via a symmetry transformation as

$$G_{HG}-G_{BC}=\dot{m}R(-Q+1,d_{HG},d_{EF},L_{HG},L_{EF},L_{BC}+d_{HG}-d_{EF};\varepsilon,\bar{c}). \tag{19b}$$

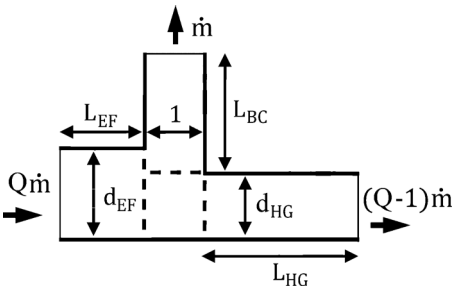

FIG. 3. The planform domain of the finite junction. All dimensions are normalized by W [Fig. 1(a)]; mass-flow rates are scaled by $2H^3p_0\rho_0/\mu$.

The above analysis is applicable to obtain an analytic approximation for R. By the boundary conditions (12) and (13), far upstream and downstream of the junction the differences between the actual values of G and those occurring in straight and uniform channels of equal respective widths approach finite limits. These limits represent the so-called minor losses[17] associated with the presence of the junction as an additional equivalent length of a uniform channel of unit (dimensionless) width. Thus, for the flow between $E_\infty F_\infty$ and $B_\infty C_\infty$ we define

$$\Delta = \lim_{x\to-\infty}\left[G-(x+1)\left(1+2\frac{\varepsilon}{d_{EF}}\bar{c}\right)\right] - \lim_{y\to\infty}[G+y(1+2\varepsilon\bar{c})]. \tag{20}$$

Making use of Eqs. (16) and (17) we evaluate these limits to obtain $\Delta\sim\Delta_0+\varepsilon\bar{c}\Delta_1$, where

$$\Delta_0=\frac{2}{\pi}\left\{Q\frac{d_{HG}}{d_{EF}}\tanh^{-1}(\sqrt{a})-d_{EF}\tan^{-1}(\sqrt{b}) + \frac{(Q-1)}{2}\ln\left[\frac{(1+b)(1-a)}{4(a+b)}\right]+\ln\left(\frac{1+b}{4\sqrt{b}}\right) + \frac{Q}{d_{EF}}\left[\frac{\pi}{2}-\tan^{-1}\left(\frac{1}{\sqrt{b}}\right)\right]+d_{HG}\tan^{-1}\left(\sqrt{\frac{b}{a}}\right)\right\} \tag{21}$$

and

$$\Delta_1=\frac{2}{\pi}\left\{\frac{\pi}{2}\left(1+\frac{Q}{d_{EF}}\right)-2Q\frac{d_{EF}-d_{HG}}{(d_{EF})^2}\tanh^{-1}(\sqrt{a}) - 2\left(d_{EF}-\frac{Q}{(d_{EF})^2}+\frac{Q}{d_{EF}}\right)\tan^{-1}(\sqrt{b}) + 2\tan^{-1}\left[\frac{\sqrt{b}(\sqrt{a}-1)}{\sqrt{a}+b}\right]+2d_{HG}\tan^{-1}\left(\sqrt{\frac{b}{a}}\right)\right\}. \tag{22}$$

The forgoing calculation applies for a junction connecting semi-infinite uniform channels. It may nevertheless be used to estimate the viscous resistance of a *finite* configuration [cf. Figs 1(b) and 3] provided that L_{EF} and L_{BC} are sufficiently large for Eqs. (12) and (13) to be approximately satisfied at the actual entrance and exit sections. Indeed, as observed in Fig. 2 (and discussed in the Appendix), uniformity of G is nearly established within a relatively small distance upstream or downstream of the junction. We thus estimate

$$R(Q,d_{EF},d_{HG},L_{EF},L_{HG},L_{BC}) \sim \Delta+Q\frac{L_{EF}}{d_{EF}}\left(1+2\varepsilon\frac{\bar{c}}{d_{EF}}\right)+L_{BC}(1+2\varepsilon\bar{c}). \tag{23}$$

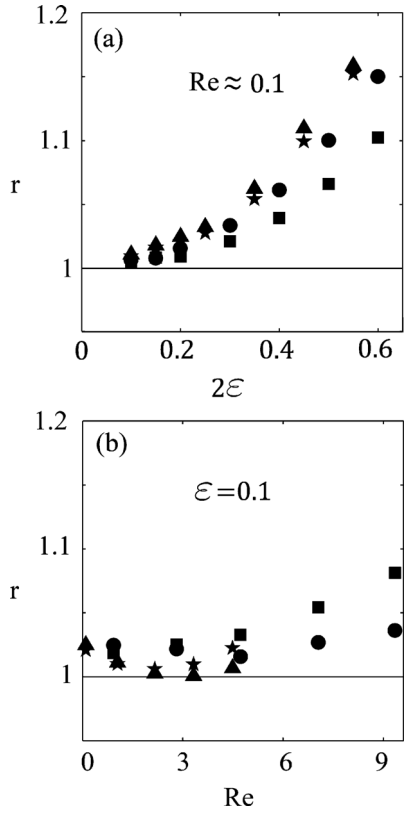

FIG. 4. Variation of r, the ratio between the values of $G_{EF}-G_{BC}$ (circles, stars) and $G_{GH}-G_{BC}$ (squares, triangles) obtained from Eq. (19) and the corresponding values obtained by numerical simulations with ε for (a) $\mathrm{Re}\leq 0.1$ and with Re for (b) $\varepsilon=0.1$. In all cases $d_{HG}=0.75$, $L_{EF}=L_{HG}=1.5$, and $L_{BC}=2$. The circles and squares mark junctions with $d_{EF}=1.25$ and the stars and triangles mark junctions with $d_{EF}=0.75$ (with $2\varepsilon=1$ corresponding to a square cross section at BC).

The above results have been tested by comparison to finite-element (COMSOL 3.4) simulations of the flow based on the full three-dimensional Navier–Stokes equations. Figure 4 presents the ratio r of the corresponding values of $G_{EF}-G_{BC}$ and $G_{GH}-G_{BC}$ obtained from the analysis and simulations for given junction geometries and mass-fluxes. A rectangular channel cross section and various values of the parameters characterizing the configuration planform were examined. Figure 4(a) confirms the quadratic $O(\varepsilon^2)$ error predicted by the analysis. Furthermore, while the present analysis assumes $\mathrm{Re}\ll 1$ effectively neglecting fluid-inertial effects, comparisons with the simulations for $\varepsilon=0.1$ [Fig. 4(b)] nevertheless demonstrate deviations smaller than 5% up to $\mathrm{Re}\leq 6$.

As mentioned in Sec. I, gas flows through microconfigurations under standard atmospheric conditions correspond to the slip-flow regime. In the above analysis the accompanying rarefaction effects are embodied in the definition (7) of G and become explicit when expressing the results in terms of

the pressure. To examine the effects of the Knudsen number we consider the variation of the reference value Kn_0 through a similarity transformation of the geometry while all entrance and exit conditions remain fixed. For a microchannel consisting of single entrance and exit sections variation of Kn_0 does not change the streamline pattern or the value of the resistance function R. Thus, with increasing Kn_0 under given entrance and exit pressures ΔG increases or, equivalently, for a prescribed ΔG the requisite pressure drop diminishes. This reflects the diminution of the viscous resistance resulting from the velocity slip at the channel walls.[14]

Contrary to the above, for a configuration consisting of multiple entrance or exit sections variation of Kn_0 modifies the streamline pattern and the viscous resistance function R. To see this we substitute the definition of G Eqs. (7) in Eq. (19) to obtain for the junction

$$\tfrac{1}{6}(p_{EF}^2 - p_{BC}^2) + \lambda Kn_0(p_{EF} - p_{BC}) = R(Q,\ldots)\dot{m} \tag{24}$$

and

$$\tfrac{1}{6}(p_{GH}^2 - p_{BC}^2) + \lambda Kn_0(p_{GH} - p_{BC}) = R(1-Q,\ldots)\dot{m}. \tag{25}$$

When varying Kn_0 while keeping entrance and exit pressures fixed, the various differences ΔG change nonuniformly (each varying according to the corresponding pressure drop). Consequently, the parameter Q representing the mass-flux distribution and (cf. Fig. 2) the corresponding streamline pattern change and so does R. From Eq. (21) to Eq. (23) we see that for a specific geometry Δ_0, Δ_1 and hence R are linear functions of Q. Making use of these in Eqs. (24) and (25) we obtain a system of algebraic equations for $\dot{m}$ and Q. The division of Eq. (24) by Eq. (25) yields Q which, unless $p_{EF}=p_{GH}$, varies nonlinearly with Kn_0. This variation is presented in Fig. 5(a) for a junction whose geometric parameters are detailed in the caption at the indicated pairs of dimensionless entrance and exit pressures. We note a significant relative variation of Q which, as can be anticipated from the above discussion, increases with increasing difference between p_{EF} and p_{GH}. Once Q has been calculated, the variation of R with Kn_0 is readily obtained from Eq. (21) to Eq. (23) [see Fig. 5(b)]. Employing these same expressions one may eliminate Q between Eqs. (24) and (25) to obtain the (linear) variation of $\dot{m}$ with Kn_0 for given pressures and geometry.

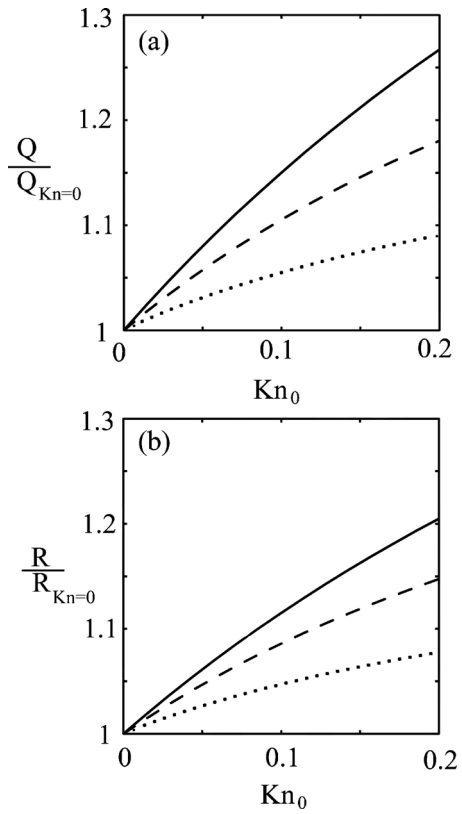

FIG. 5. Variation with Kn_0 of (a) Q, the mass-flux distribution parameter and (b) R, the viscous resistance, normalized by their corresponding values at $Kn_0=0$. The junction geometry is defined by $d_{EF}=1$, $d_{HG}=0.75$, $L_{EF}=L_{HG}=2$, and $L_{BC}=3$. The normalized pressures are $p_{BC}=1$ and $(p_{EF},p_{GH})=(1.5,0.5$; solid lines), (1.25,0.75; dashed lines) and (1.1,0.9; dotted lines).

III. AN ILLUSTRATION: PARALLEL-CHANNEL NETWORK

We now apply the above analysis to study the flow in gas distribution systems such as the one schematically depicted in Fig. 6, consisting of N parallel (vertical) channels connecting the feed and drain (horizontal) channels. A common optimization requirement[7–9,18] is to have equal mass-flow rates through the N parallel channels. For the present illustration we consider a system formed by placing between the top and bottom plates the (hatched) $N-1$ identical evenly spaced rectangular parallelepiped obstacles. Thus, the entire configuration is specified with the exception of the gap widths w_k $(k=1,2,\ldots,N-1)$ which are to be selected so as to satisfy the above flux-uniformity criterion.

We have noted in Fig. 2 that G becomes nearly uniform across the channel width within a relatively short distance upstream or downstream of the junction. Provided that such uniformity is also achieved in the present application (see the Appendix) we may neglect hydrodynamic interactions between adjacent junctions and use the results of the preceding section to estimate the performance of the entire network through adding up separate contributions of junction elements (as the one marked by the shaded area in Fig. 6).

By equating the respective pressure drops along all paths

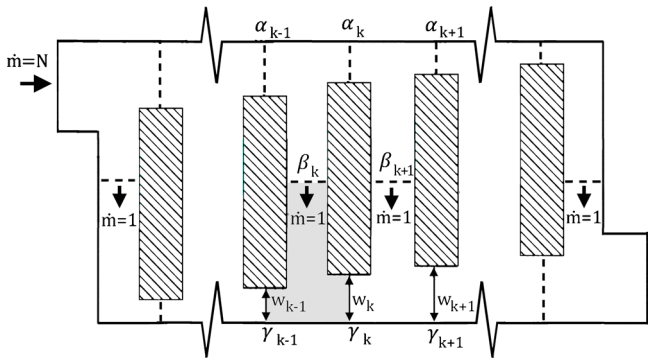

FIG. 6. (Color online) A schematic description of a parallel-channel gas distributor.

from the inlet to the outlet sections we obtain the system of $N-1$ equations

$$[G(\gamma_k) - G(\beta_k)] + [G(\beta_{k+1}) - G(\gamma_k)] = [G(\alpha_k) - G(\beta_k)] + [G(\beta_{k+1}) - G(\alpha_k)], \quad (k = 1,2 \ldots N-1). \tag{26}$$

From the above discussion, each of the differences in square brackets may then be approximated by a relation similar to Eq. (23) while requiring equal mass-flow rates through all of the parallel channels. For instance the first term of the left-hand side of Eq. (26) representing the effect of the shaded junction is

$$[G(\gamma_k) - G(\beta_k)] = \dot{m}R(w_{k-1}, w_k, \ldots), \tag{27}$$

where the explicit dependence of R upon all other (*a priori* known) parameters has been omitted. Making use of Eqs. (20)–(23) we obtain from Eq. (26) a system of $N-1$ equations for the unknowns w_k $(k=1,2,\ldots,N-1)$.

The calculation is illustrated for the distribution system consisting of four parallel channels depicted in Fig. 7. The dimensionless widths of all parallel channels and rectangular obstacles are equal to unity. The normalized lengths of the latter are equal to 8.5 and the corresponding dimension of the entire system is 10. The widths of the entrance and exit sections are both equal to 1.5. Presented in the figure are the streamline (solid lines) and isobar (dashed lines) patterns for the flow of air when $H=1$ μm, $\varepsilon=0.1$ and $\mathrm{Re}\approx 0.1$ as obtained via finite-element (COMSOL 3.4) simulations. In part (a) all w_k are equal whereas in part (b) they are obtained from the solution of Eq. (26). Focusing on the bold streamlines dividing the system into four domains of equal mass-flow rates, we see that in part (a) of the figure the mass flow rates through the side channels are significantly larger those through the middle pair. Turning to part (b), it is evident that the present procedure results in the required uniformity. The same conclusions result from examining the density of the equidistant isobars in conjunction with Eq. (8) for the mass-flux density. The simulation results indicate that relative deviations between the mass flow rates through the various parallel channels are within 1%. (A useful byproduct of the optimization requirement is a 6% increase in the total mass flow rate for given entrance and exit conditions.)

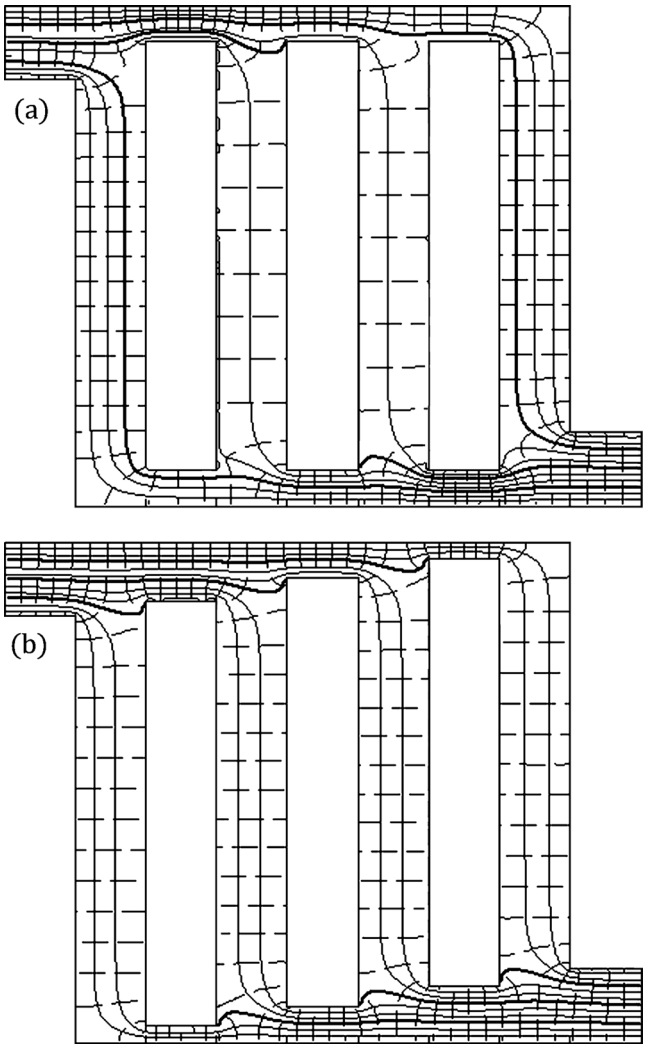

FIG. 7. Midplane streamline (solid lines) and isobar (dashed lines) patterns in a model shallow parallel microchannel network. The bold solid lines mark the division into four equal portions of the total mass-flux. The figure presents (a) a network in which w_k are uniform, (b) an optimized configuration calculated by use of Eq. (26). The simulation is of air flow for $H=1$ μm, $\varepsilon=0.1$, and $\mathrm{Re}\approx 0.1$ (based on configuration depth). Values of the geometric parameters are detailed in the text.

IV. CONCLUDING REMARKS

Our recent extension of the asymptotic Hele-Shaw scheme has been applied to analyze gas flows through T-junctions connecting shallow microchannels. The linearity of the problem in terms of G, the quadratic form of the pressure [Eq. (7)], allows for the definition of the viscous resistance as an intrinsic property of the configuration. Furthermore, under rather mild restrictions, the performance of complex systems (e.g., microchannel networks) may readily be estimated through adding up the contributions of simple basic (junctions) elements (similarly to the calculation of electric circuits). While simulation of the flow through any given configuration is, in principle, rather straightforward, mapping of the entire multidimensional parameter space may become prohibitively tedious. The present scheme thus presents a useful alternative in the preliminary design and optimization of microfluidic devices.

APPENDIX: RELAXATION TO A UNIFORM FLOW ACROSS STRAIGHT-CHANNEL SEGMENTS

1. Calculation of *G*

Consider a straight and uniform channel segment of dimensionless length l. The leading-order G_0 satisfies Eq. (10a) for $0\le x\le l$ and $0\le y\le 1$ together with the homogeneous conditions [Eq. (11a)] at $y=0,1$ and the conditions

$$\frac{\partial G_0}{\partial x} = \begin{cases} f_1^{(0)}(y) & \text{at } x=0 \\ f_2^{(0)}(y) & \text{at } x=l \end{cases}, \tag{A1}$$

where $f_{1,2}(y)$, which satisfy $\int_0^1 f_1(y)dy = \int_0^1 f_2(y)dy$ to ensure well posedness of the above Neumann problem, are other-

wise arbitrary distributions. Separation of variables readily yields the solution

$$G_0 = A_0^{(0)} x + C^{(0)} + \sum_{n=1}^{\infty} \{A_n^{(0)} \cosh(n\pi x) + B_n^{(0)} \cosh[n\pi(l-x)]\} \cos(n\pi y), \quad \text{(A2)}$$

where $C^{(0)}$ is an arbitrary constant, $A_0^{(0)} = \int_0^1 f_1^{(0)}(y)dy$ and

$$[A_n^{(0)}, B_n^{(0)}] = \frac{2}{n\pi \sin(n\pi l)} \int_0^1 [f_2^{(0)}(y_1), -f_1^{(0)}(y_1)] \times \cos(n\pi y_1) dy_1. \quad \text{(A3)}$$

From these we see that the nonuniform (y-dependent) parts of G_0 behave like

$$\frac{\cosh(n\pi x)}{\sinh(n\pi l)} \sim e^{-n\pi(l-x)} \quad \text{and} \quad \frac{\cosh[n\pi(l-x)]}{\sinh(n\pi l)} \sim e^{-n\pi x}, \quad \text{(A4)}$$

respectively, i.e., they essentially decay within a single channel width from the entrance ($x=0$) and exit ($x=l$) sections.

The correction term G_1 is governed by Eq. (10b) in conjunction with $\partial G_1/\partial y = \partial^2 G_0/\partial x^2$ at $y=0,1$ [Eq. (11b)] as well as entrance and exit conditions similar to Eq. (A1) where the distributions $f_1^{(0)}(y)$ and $f_2^{(0)}(y)$ are replaced by $f_1^{(1)}(y)$ and $f_2^{(1)}(y)$, respectively. To calculate G_1 we present it as the sum

$$G_1 = G_{11} + \sum_{n=1}^{\infty} n\pi \{A_n^{(0)} \cosh(n\pi x) + B_n^{(0)} \cosh[n\pi(l-x)]\} \sin(n\pi y), \quad \text{(A5)}$$

where $A_n^{(0)}$ and $B_n^{(0)}$ are given in Eq. (A3) and G_{11} satisfies a Neumann problem similar to that governing G_0 where $f_i^{(0)}(y)$ $(i=1,2)$ appearing on the right-hand side of Eq. (A1) are now replaced by $f_i^{(1)} - 2\Sigma_{n=1}^{\infty} f_i^{(0)}(y_1)\cos(n\pi y_1)dy_1 \sin(n\pi y_1)$ $(i=1,2)$. Thus similarly to Eq. (A4), the y-dependent parts of G_{11} decay exponentially rapidly with increasing distance from the entrance and exit sections.

2. The flow through a channel segment connecting a pair of adjacent junctions

To further clarify the relaxation to uniformity in the context of parallel-channel networks we have simulated the flow through a configuration consisting of a pair of junctions in close proximity, schematically depicted by the inset in Fig. 8. In these simulations the indicated passage width w has been varied while keeping all other configuration parameters fixed. The figure presents the approach to uniformity of the pressure distribution over the cross section marked by the dashed line halfway between the adjacent junctions. This is described through the decrease with l/w of σ, the standard deviation of the pressure distribution (normalized by the smaller of the total pressure drops between this and each of the downstream exit sections). Evidently, for $l/w \geq 1$ σ is negligibly small (in fact it is already less than $\approx 10^{-2}$ for $l/w > 2/3$). Further evidence in support of the neglect of hydrodynamic interactions is provided by Yu *et al.*[19] who studied gas flows through multicavity shallow microchannels. Specifically, they observed that, once the distance between adjacent cavities exceeded the length of a single cavity, the total effect on mass-flow rate was linear in the number of cavities.

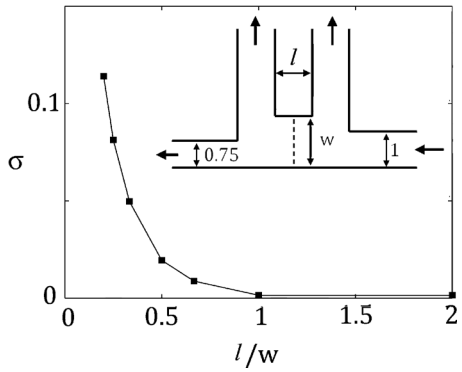

FIG. 8. Variation with the ratio l/w of σ, the standard deviation of the pressure distribution across the channel section halfway between the adjacent parallel channels (indicated by the dashed line in the inset).

[1] S. K. Griffiths and R. H. Nilson, "Low-dispersion turns and junctions for microchannel systems," Anal. Chem. **73**, 272 (2001).
[2] S. H. Wong, M. C. L. Ward, and C. W. Wharton, "Micro T-mixer as a rapid mixing micromixer," Sens. Actuators B **100**, 359 (2004).
[3] Y. Ma, C.-P. Sun, M. Fields, Y. Li, D. Haake, B. Churchill, and C.-M. Ho, "An unsteady microfluidic T-form mixer perturbed by hydrodynamic pressure," J. Micromech. Microeng. **18**, 045015 (2008).
[4] D. Qian and A. Lawal, "Numerical study on gas and liquid slugs for Taylor flow in a T-junction microchannel," Chem. Eng. Sci. **61**, 7609 (2006).
[5] M. D. Menech, P. Garstecki, F. Jousse, and H. A. Stone, "Transition from squeezing to dripping in a microfluidic T-shaped junction," J. Fluid Mech. **595**, 141 (2008).
[6] K.-L. Lao, J.-H. Wang, and G.-B. Lee, "A microfluidic platform for formation of double-emulsion droplets," Microfluid. Nanofluid. **7**, 709 (2009).
[7] A. Aricò, P. Creti, V. Baglio, E. Modica, and V. Antonucci, "Influence of flow field design on the performance of a direct methanol fuel cell," J. Power Sources **91**, 202 (2000).
[8] S. Karvonen, T. Hottinen, J. Saarinen, and O. Himanen, "Modeling of flow field in polymer electrolyte membrane fuel cell," J. Power Sources **161**, 876 (2006).
[9] Y. Ferng and A. Su, "A three dimensional full-cell CFD model used to investigate the effects of different flow channel designs on PEMFC performance," Int. J. Hydrogen Energy **32**, 4466 (2007).
[10] J. M. MacInnes, X. Du, and R. W. K. Allen, "Prediction of electrokinetic and pressure flow in a microchannel T-junction," Phys. Fluids **15**, 1992 (2003).
[11] N. Fujisawa, Y. Nakamura, F. Matsuura, and Y. Sato, "Pressure field evaluation in microchannel junction flows through μPIV measurement," Microfluid. Nanofluid. **2**, 447 (2006).
[12] E. B. Arkilic, M. A. Schmidt, and K. S. Breuer, "Gaseous slip flow in long microchannels," J. Microelectromech. Syst. **6**, 167 (1997).
[13] Y. Zohar, S. Y. Lee, W. Y. Lee, L. Jiang, and P. Tong, "Subsonic gas flow in a straight and uniform microchannel," J. Fluid Mech. **472**, 125 (2002).
[14] C. Cercignani, *Rarefied Gas Dynamics* (Cambridge University Press, Cambridge, 2000).
[15] A. D. Gat, I. Frankel, and D. Weihs, "A higher-order Hele-Shaw approximation with application to gas flows through shallow microchannels," J. Fluid Mech. **638**, 141 (2009).

[16]A. Gat, I. Frankel, and D. Weihs, "Gas flows through constricted shallow microchannels," J. Fluid Mech. **602**, 427 (2008).
[17]F. M. White, *Fluid Mechanics*, 2nd ed. (McGraw-Hill, New York, 1986).
[18]W. Zhang, P. Hu, X. Lai, and L. Peng, "Analysis and optimization of flow distribution in parallel-channel configurations for proton exchange membrane fuel cells," J. Power Sources **194**, 931 (2009).
[19]Z. T. F. Yu, Y.-K. Lee, M. Wong, and Y. Zohar, "Fluid flows in microchannels with cavities," J. Microelectromech. Syst. **14**, 1386 (2005).